NPS-ME-98-005

NAVAL POSTGRADUATE SCHOOL
Monterey, California

Development of a Shell Element with Pressure Variation through the Thickness - Part II

by
Patrick M. McDermott
Young W. Kwon

01 October, 1997 - 30 September, 1998

Approved for public release; distribution is unlimited.

Prepared for: Naval Surface Warfare Center
Carderock, MD 20817

Naval PostGraduate School
Monterey, California

Rear Admiral R. C. Chaplin
Superintendent

R. S. Elster
Provost

This report was prepared in conjuction with research conducted for Naval Surface Warfare Center, Carderock Division

The report was prepared by:

Patrick M. McDermott
Lieutenant, United States Navy

and

Young W. Kwon
Associate Professor of Mechanical Engineering

Reviewed by:

T. R. McNelley
Chairman
Department of Mechanical Engineering

Released by:

D. W. Netzer
Dean of Research

REPORT DOCUMENTATION PAGE

Form Approved OMB No. 0704-0188

1. AGENCY USE ONLY *(Leave blank)*	2. REPORT DATE	3. REPORT TYPE AND DATES COVERED
	30 September, 1998	Progress Report 10/97 to 9/98

4. TITLE AND SUBTITLE
Development of a Shell Element with Pressure Variation Through the Thickness - Part II

5. FUNDING NUMBERS
N00167-97-WR-70463

6. AUTHOR(S) Patrick M. McDermott and Young W. Kwon

7. PERFORMING ORGANIZATION NAME(S) AND ADDRESS(ES)
Naval Postgraduate School
Monterey CA 93943-5000

8. PERFORMING ORGANIZATION REPORT NUMBER
NPS-ME-98-005

8. SPONSORING/MONITORING AGENCY NAME(S) AND ADDRESS(ES)
Naval Surface Warfare Center, Carderock Division
West Bethesda, Maryland 20817-5700

10. SPONSORING/ MONITORING AGENCY REPORT NUMBER

11. SUPPLEMENTARY NOTES The views expressed in this thesis are those of the author and do not reflect the official policy or position of the Department of Defense or the U.S. Government.

12a. DISTRIBUTION/AVAILABILITY STATEMENT
Approved for public release; distribution is unlimited.

12b. DISTRIBUTION CODE
A

13. ABSTRACT ***(maximum 200 words)***

A shell formulation was developed from a three-dimensional solid. The shell element is isoparametric and has four corner nodes at which there are three independent displacements and three independent rotations. The element formulation includes both transverse shear and transverse normal deformations. The element utilizes reduced integration along the in-plane axes and full integration along the transverse axis. The formulation incorporates the Gurson constitutive model for void growth and plastic deformation. Hourglass mode control is provided by adding a small fraction of internal force determined through full integration along the in-plane axes and reduced integration along the transverse axis.

14. SUBJECT TERMS
Finite Element Method, Shell Formulation, High Order Element, Void Model

15. NUMBER OF PAGES 47

16. PRICE CODE

17. SECURITY CLASSIFICATION OF REPORT	18. SECURITY CLASSIFICATION OF THIS PAGE	19. SECURITY CLASSIFICATION OF ABSTRACT	20. LIMITATION OF ABSTRACT
Unclassified	Unclassified	Unclassified	UL

ABSTRACT

A shell formulation was developed from a three-dimensional solid. The shell element is isoparametric and has four corner nodes at which there are three independent displacements and three independent rotations. The element formulation includes both transverse shear and transverse normal deformations. The element utilizes reduced integration along the in-plane axes and full integration along the transverse axis. The formulation incorporates the Gurson constitutive model for void growth and plastic deformation. Hourglass mode control is provided by adding a small fraction of internal force determined through full integration along the in-plane axes and reduced integration along the transverse axis.

TABLE OF CONTENTS

1. INTRODUCTION

The Naval Surface Warfare Center (NSWC), in collaboration with Germany, has developed a computer simulation program, (DYSMAS), to model both the linear and nonlinear behavior of ship structures under shock loading. This program is targeted towards computer simulation of U.S Navy ship shock trials. The failure process must be modeled in an accurate and reliable way in order to meet the objectives of this program. One effort to model this nonlinear failure process is to implement damage constitutive equations, like Gurson's void model, into the program.

Shell elements are used for modeling since the major structure in a ship is a shell. The formulation of this shell element must include damage constitutive equations. The element must accurately reflect the elastic-plastic transition in a dynamic environment. Therefore, the overall objective of this research is to develop a shell element which can include the damage constitutive equations.

The first phase of the research developed a shell element which can include Gurson's void model at the next phase. Since Gurson's void model uses hydrostatic pressure (mean stress) and deviatoric stress, these values must be available. The second phase is to implement the void model into the shell formulation developed in the first phase. The final phase is to incorporate the entire module into the DYSMAS program. Each phase requires extensive verification of the developed shell element.

The first phase was completed in September, 1997. All applicable portions of the report covering the first phase are repeated in this report, since some of the procedures outlined there had to be modified to implement Gurson's void model [1]. This report covers the work of both the first and second phases.

2. FINITE ELEMENT FORMULATION

2.1 Geometry

A point in a shell structure can be expressed by a vector sum of two vectors. The first vector is a position vector from the origin of the coordinate system to a point on a reference surface of the shell element. The second vector is a position vector from this reference surface to the point under consideration. The surface that spans the center of the transverse axis is used as the reference surface in this formulation, although any surface would suffice. The first vector terminates at the reference surface directly below the point in question. The second vector is then the normal from the reference surface that intersects the desired point. Figure 1 shows this relationship.

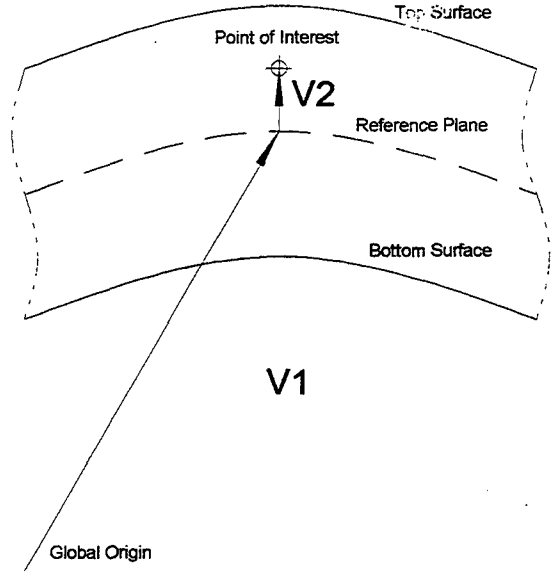

Figure 1. Element Cross-section.

Two shape functions are used to describe a position in the element; N^k is the two dimensional shape function in the ξ-η plane, and H^k is the one dimensional shape function along the ζ axis, where (ξ,η,ζ) describes a point in the natural coordinate system. A generic point of a shell may now be described in terms of the position vectors of the nodes and the shape functions:

$$x_i(\xi,\eta,\zeta) = \sum_{k=1}^{n} N^k(\xi,\eta)\, x_i^k + \sum_{k=1}^{n} N^k(\xi,\eta) H^k(\zeta) V_{3i}^k \quad (i = 1,2,3) \tag{1}$$

where x_i^k is the position vector of node k in the reference surface; V_{3i}^k is the unit vector at the node k; and n is the number of nodes per element. In the present formulation, a four-node shell element is considered. The unit vector V_{3i}^k is defined as

$$V_{3i}^k = \frac{(x_i^k)^{top} - (x_i^k)^{bottom}}{\left\| (x_i^k)^{top} - (x_i^k)^{bottom} \right\|} \tag{2}$$

where *top* and *bottom* indicate the top and bottom surfaces of the shell, and $\| \ \|$ denotes the Euclidean norm. The one-dimensional shape function H^k is expressed as

$$H^k(\zeta) = \left[\frac{1}{4}(1+\zeta)(1-\bar{\zeta}) - \frac{1}{4}(1-\zeta)(1+\bar{\zeta}) \right] \left\| (x_i^k)^{top} - (x_i^k)^{bottom} \right\| \tag{3}$$

in which $\bar{\zeta}$ indicates the location of the reference surface and varied from -1 to 1 ($\bar{\zeta} = 0$ denotes the mid-surface). The two-dimensional shape function N^k is expressed as

$$\begin{aligned} N^1 &= \tfrac{1}{4}(1-\xi)(1-\eta) \\ N^2 &= \tfrac{1}{4}(1+\xi)(1-\eta) \\ N^3 &= \tfrac{1}{4}(1+\xi)(1+\eta) \\ N^4 &= \tfrac{1}{4}(1-\xi)(1+\eta) \end{aligned} \tag{4}$$

2.2 Displacement

The displacement field in a shell can be written as

$$u_i(\xi,\eta,\zeta) = \sum_{k=1}^{n} N^k(\xi,\eta) u_i^k + \sum_{k=1}^{n} N^k(\xi,\eta) H^k(\zeta)(-V_{2i}^k\theta_{1i}^k + V_{1i}^k\theta_{2i}^k + V_{3i}^k\theta_{3i}^k) \quad (i = 1,2,3) \textbf{(5)}$$

in which u_i is the displacement along the x_i axis, u_i^k is the nodal displacement at the node k, and unit vectors V_{1i}^k and V_{2i}^k lie along the reference surface. V_{1i}^k, V_{2i}^k and V_{3i}^k are perpendicular to one another. θ_{1i}^k, θ_{2i}^k and θ_{3i}^k are rotational degrees of freedom along the unit vectors V_{1i}^k, V_{2i}^k and V_{3i}^k, respectively. The right-hand rule is assumed for the positive direction of each rotation. Figure 2 illustrates the relationship among these vectors.

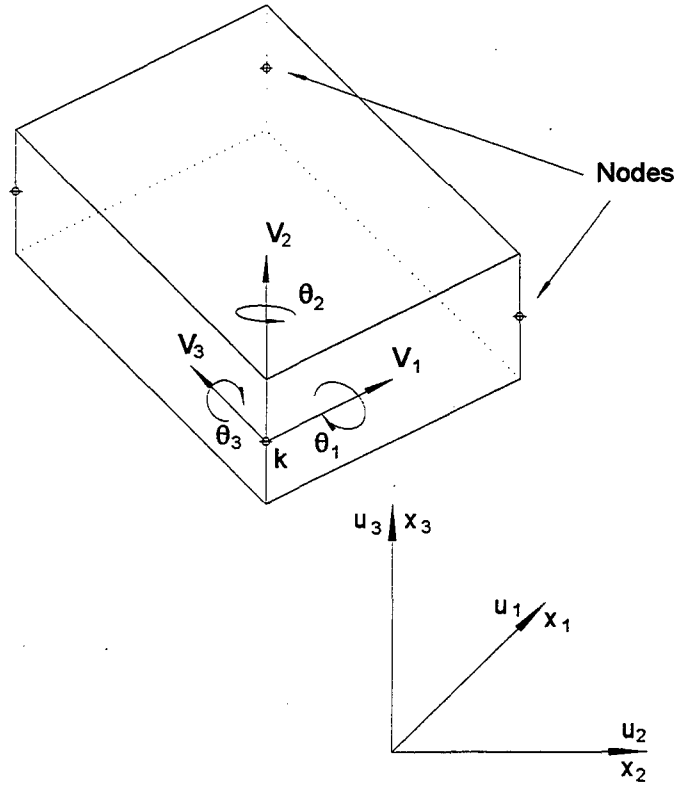

Figure 2. Displacement Vector Orientation.

θ_{1i}^k and θ_{2i}^k are the bending rotations, while θ_{3i}^k is the drilling rotational degree of freedom. The role of θ_{3i}^k can be clarified by considering a flat plate parallel to the x_1x_2 plane. Now Equation (5) can be rewritten as

$$u_i = u_i^{mid} + x_3\theta_i \quad (i = 1,2,3) \tag{6}$$

where u_1 and u_2 are the inplane displacements, and u_3 is the transverse displacement. The superscript *mid* indicates the mid-plane of the plate. Equation (6) demonstrates that the transverse displacement is not constant through the plate thickness (i.e. along the x_3 axis). Therefore, the transverse normal strain is included in this formulation, along with the transverse shear strains.

In the implementation, the unit direction vectors are fixed to the first node listed in the element, where the nodes are ordered in a counter-clockwise direction, as shown in Figure 3. V_3 is normal to the plane formed by nodes 1, 2, and 4. V_2 lies along the line connecting nodes 1 and 4. V_1 is normal to the plane formed by V_2 and V_3. This means that V_1 will not, in general, lie along the line connecting nodes 1 and 2. For each node, the following information is stored at each time step: displacement (d_x, d_y, d_z, θ_x, θ_y, θ_z), velocity (v_x, v_y, v_z, $\dot{\theta}_x$, $\dot{\theta}_y$, $\dot{\theta}_z$), and acceleration (a_x, a_y, a_z, $\ddot{\theta}_x$, $\ddot{\theta}_y$, $\ddot{\theta}_z$). Using a four-node element, each node has six degrees of freedom (dof), and each element has 24 dof's in displacement, velocity, and acceleration.

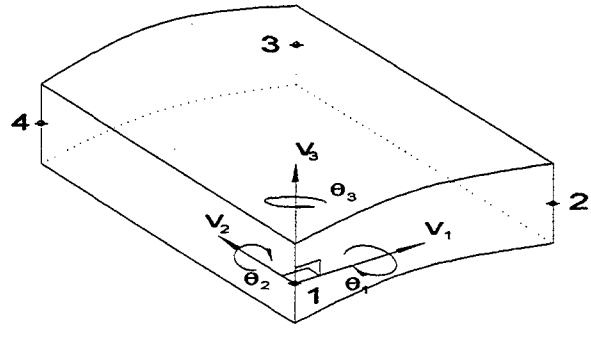

Figure 3. Node Number and Unit Direction Vector Scheme.

2.3 Coordinate Transformation

Combining the three unit direction vectors into matrix T_p provides the rotation transformation matrix, or matrix of direction cosines, as shown in Equation (7). T_p^{-1} is used to transform the nodal angular displacements from the global coordinate system to local coordinates, as shown in Equation (8), where k is the node number. Once the internal force vector is generated in local, T_p is used to transform the moments back into global coordinates. This procedure is discussed later in section 2.7.

$$T_p = \left| \vec{V}_1 \ \vec{V}_2 \ \vec{V}_3 \right|_{(3x3)} \tag{7}$$

$$\{d^k\}_{(6x1)} = \begin{vmatrix} 1 & 0 & 0 & 0 & 0 & 0 \\ 0 & 1 & 0 & 0 & 0 & 0 \\ 0 & 0 & 1 & 0 & 0 & 0 \\ 0 & 0 & 0 & & & \\ 0 & 0 & 0 & & [T_p^{-1}] & \\ 0 & 0 & 0 & & & \end{vmatrix} \left\{ d^k_{global} \right\}_{(6x1)} \quad (k = 1,2,3,4) \tag{8}$$

The strain transformation matrix, T, is used to transform calculated strain from the global coordinate system to local coordinates. Transforming the resulting stress from local coordinates to the global coordinate system would normally require using T^{-1}, but since T is orthogonal, $T^{-1} = T^T$, where T^T is the transpose of T. This property negates the requirement to invert a six by six matrix. For a detailed derivation of these transformations, refer to Cook [2]. The strain transformation matrix is explicitly defined in Equation (9), where V_{ij} is the cosine of the direction vector V_i in the x_j direction. Both of these transformation matrices are calculated once per element per time step.

$$
\boldsymbol{T} = \begin{bmatrix}
V_{11}^2 & V_{12}^2 & V_{13}^2 & V_{11}V_{12} & V_{12}V_{13} & V_{11}V_{13} \\
V_{21}^2 & V_{22}^2 & V_{23}^2 & V_{21}V_{22} & V_{22}V_{23} & V_{21}V_{23} \\
V_{31}^2 & V_{32}^2 & V_{33}^2 & V_{31}V_{32} & V_{32}V_{33} & V_{31}V_{33} \\
2V_{11}V_{21} & 2V_{12}V_{22} & 2V_{13}V_{23} & V_{11}V_{22}+V_{21}V_{12} & V_{12}V_{23}+V_{22}V_{13} & V_{13}V_{21}+V_{23}V_{11} \\
2V_{21}V_{31} & 2V_{22}V_{32} & 2V_{23}V_{33} & V_{21}V_{32}+V_{31}V_{22} & V_{22}V_{33}+V_{32}V_{23} & V_{23}V_{31}+V_{33}V_{21} \\
2V_{11}V_{31} & 2V_{12}V_{32} & 2V_{13}V_{33} & V_{11}V_{32}+V_{31}V_{12} & V_{12}V_{33}+V_{32}V_{13} & V_{13}V_{31}+V_{33}V_{11}
\end{bmatrix} \quad \textbf{(9)}
$$

2.4 Strain Displacement Relation

The six components of the strain tensor are computed from Equation (5) by taking its derivative with respect to the x_i axis. In matrix form, the result for a four-node element is:

$$\{\epsilon\} = [B]\{d\} \quad \textbf{(10)}$$

where

$$\{\epsilon\} = \{\epsilon_{11}\ \epsilon_{22}\ \epsilon_{33}\ \gamma_{12}\ \gamma_{23}\ \gamma_{13}\}^T \quad \textbf{(11)}$$

$$[B] = [B^1\ B^2\ B^3\ B^4] \quad \textbf{(12)}$$

$$\{d\} = \{d^1\ d^2\ d^3\ d^4\}^T \quad \textbf{(13)}$$

The detailed expression for $[B^k]$ is

$$[B^k] = \begin{bmatrix} \frac{\partial N^k}{\partial x_1} & 0 & 0 & -g_1^k V_{21}^k & g_1^k V_{11}^k & g_1^k V_{31}^k \\ 0 & \frac{\partial N^k}{\partial x_2} & 0 & -g_2^k V_{22}^k & g_1^k V_{12}^k & g_1^k V_{32}^k \\ 0 & 0 & \frac{\partial N^k}{\partial x_3} & -g_1^k V_{23}^k & g_1^k V_{13}^k & g_1^k V_{33}^k \\ \frac{\partial N^k}{\partial x_2} & \frac{\partial N^k}{\partial x_1} & 0 & -g_2^k V_{21}^k - g_1^k V_{22}^k & g_2^k V_{11}^k + g_1^k V_{12}^k & g_2^k V_{31}^k + g_1^k V_{32}^k \\ 0 & \frac{\partial N^k}{\partial x_3} & \frac{\partial N^k}{\partial x_2} & -g_k^k V_{22}^k - g_k^k V_{23}^k & g_k^k V_{12}^k + g_k^k V_{13}^k & g_k^k V_{32}^k + g_k^k V_{33}^k \\ \frac{\partial N^k}{\partial x_3} & 0 & \frac{\partial N^k}{\partial x_1} & -g_3^k V_{21}^k - g_1^k V_{23}^k & g_3^k V_{11}^k + g_1^k V_{13}^k & g_3^k V_{31}^k + g_1^k V_{33}^k \end{bmatrix} \quad \textbf{(14)}$$

in which

$$g_i^k = \frac{\partial N^k}{\partial x_i} H^k + N^k \frac{\partial H^k}{\partial x_i} \quad \textbf{(15)}$$

The vector $\{d^k\}$ is defined as

$$\{d^k\} = \left\{ u_1^k \; u_2^k \; u_3^k \; \theta_1^k \; \theta_2^k \; \theta_3^k \right\} \quad \textbf{(16)}$$

where u_i is the displacement along the x_i direction at node k, and θ_i is the rotational displacement about the x_i axis at node k. The matrix $[B^k]$ must be calculated for each integration point. The stress tensor, discussed later, is also stored as a vector.

2.5 Jacobian Matrix

Computing the derivatives $\frac{\partial N^k}{\partial x_i}$ and $\frac{\partial H^k}{\partial x_i}$ requires the Jacobian matrix, defined as

$$[J] = \begin{bmatrix} x_{1,\xi} & x_{2,\xi} & x_{3,\xi} \\ x_{1,\eta} & x_{2,\eta} & x_{3,\eta} \\ x_{1,\zeta} & x_{2,\zeta} & x_{3,\zeta} \end{bmatrix} \tag{17}$$

where

$$\frac{\partial x_i}{\partial \xi} = \sum_{k=1}^{n} \frac{\partial N^k}{\partial \xi} x_i + \sum_{k=1}^{n} \frac{\partial N^k}{\partial \xi} H^k V_{3i}^k \quad (i = 1,2,3) \tag{18}$$

$$\frac{\partial x_i}{\partial \eta} = \sum_{k=1}^{n} \frac{\partial N^k}{\partial \eta} x_i + \sum_{k=1}^{n} \frac{\partial N^k}{\partial \eta} H^k V_{3i}^k \quad (i = 1,2,3) \tag{19}$$

$$\frac{\partial x_i}{\partial \zeta} = \sum_{k=1}^{n} N^k \frac{\partial H^k}{\partial \zeta} V_{3i}^k \quad (i = 1,2,3) \tag{20}$$

$[R]$ is defined as the inverse of the Jacobian ($\mathbf{J}^{-1}$). Then the required partial derivatives are defined as

$$\frac{\partial N^k}{\partial x_i} = R_{i1} \frac{\partial N^k}{\partial \xi} + R_{i2} \frac{\partial N^k}{\partial \eta} \quad (i = 1,2,3) \tag{21}$$

$$\frac{\partial H^k}{\partial x_i} = R_{i3} \frac{\partial H^k}{\partial \zeta} \quad (i = 1,2,3) \tag{22}$$

Both the Jacobian and its inverse are calculated at each integration point for each time step. The inverse of the three by three matrix **J** is explicitly calculated (no loops).

2.6 Stress-Strain Relationship

The strain calculated in Equation (10) is in global coordinates, and is transformed to the local coordinate system using

$$\{\epsilon_{local}\} = [\boldsymbol{T}]\{\epsilon_{global}\} \tag{23}$$

where $[\boldsymbol{T}]$ is defined in Equation (9). Stress is calculated from the strain (local coordinates) using the plane-strain formulas:

$$\begin{aligned} \sigma_{x'} &= \frac{E}{1-\nu^2}(\epsilon_x + \nu\epsilon_y) & \tau_{x'y'} &= G\gamma_{xy} \\ \sigma_{y'} &= \frac{E}{1-\nu^2}(\nu\epsilon_x + \epsilon_y) & \tau_{y'z'} &= \mathrm{K}G\gamma_{yz} \\ \sigma_{z'} &= E\epsilon_z & \tau_{x'z'} &= \mathrm{K}G\gamma_{xz} \end{aligned} \tag{24}$$

where K is the shear correction factor, E is the elastic modulus, G is the shear modulus, and ν is Poisson's ratio. The resulting stresses are in the local coordinate system and are converted to the global coordinate system with

$$\{\sigma\} = [T]^T\{\sigma'\} \tag{25}$$

$$\{\sigma\} \equiv \{\sigma_x\ \sigma_y\ \sigma_z\ \gamma_{xy}\ \gamma_{yz}\ \gamma_{xz}\} \tag{26}$$

where **T** is from Equation (9).

2.7 Internal Force, Mass, and Assembly into System Matrix

The stress resulting from Equation (25) is then converted to an internal force vector and summed over all integration points using

$$\{f_{internal}\} = \int_{-1}^{1}\int_{-1}^{1}\int_{-1}^{1} [B]^T\{\sigma\}d\xi d\eta d\zeta = \sum_{i=1}^{nx}\sum_{j=1}^{ny}\sum_{k=1}^{nz} [B]^T\{\sigma\}w_i w_j w_k|J| \qquad (27)$$

where | **J** | is the determinant of the Jacobian matrix, *nx*, *ny*, and *nz* are the number of integration points in the x_1, x_2, and x_3 directions, respectively, and w_i, w_j, and w_k, are the Gauss weights for those directions. The resulting force vector, $\{f_{int}\}$, must have its moments transformed back to the global coordinate system using

$$\{F_{int}^k\}_{(6x1)} = \begin{vmatrix} 1 & 0 & 0 & 0 & 0 & 0 \\ 0 & 1 & 0 & 0 & 0 & 0 \\ 0 & 0 & 1 & 0 & 0 & 0 \\ 0 & 0 & 0 & & & \\ 0 & 0 & 0 & & [T_p] & \\ 0 & 0 & 0 & & & \end{vmatrix} \{f_{int}^k\}_{(6x1)} \quad (k = 1,2,3,4) \qquad (28)$$

A lumped mass method is used for the element mass matrix. The matrix is diagonal, with each diagonal element the same:

$$[M_e] = \begin{bmatrix} m_e & 0 & 0 & \dots & 0 \\ 0 & m_e & 0 & \dots & 0 \\ 0 & 0 & m_e & \dots & 0 \\ \dots & \dots & \dots & \dots & \dots \\ 0 & 0 & 0 & \dots & m_e \end{bmatrix} \qquad (29)$$

where

$$m_e = \frac{\left(\sum_{i=1}^{nx} \sum_{j=1}^{ny} \sum_{k=1}^{nz} w_i w_j w_k |J| \right) \rho}{n} \tag{30}$$

with $n = 4$ in this four-node element. Using a diagonal mass matrix greatly simplifies time integration, since inverting it is trivial and takes little computation time. The internal force vector and element mass vector (each 24 by 1) are then assembled into the corresponding system vectors, each of which is a column vector having one row for each dof.

3. EXPLICIT TIME INTEGRATION

The use of internal force vectors and explicit time integration negates the need to explicitly form the element and system stiffness matrices. The acceleration vector is computed from

$$\{\ddot{U}\}^t = [M]^{-1}\left(\{F_{ext}\}^t - \{F_{int}\}^t\right) \tag{31}$$

where $\{\ddot{U}\}$ is the system acceleration vector, $[M]$ is the system mass matrix, $\{F_{ext}\}$ is the system external force vector, and superscript t denotes the time step. Velocity and displacement are then quickly found using

$$\begin{aligned} \{\dot{U}\}^{t+\frac{\Delta t}{2}} &= \{\dot{U}\}^{t-\frac{\Delta t}{2}} + \{\ddot{U}\}^t \Delta t \\ \{U\}^{t+\Delta t} &= \{U\}^t + \{\dot{U}\}^{t+\frac{\Delta t}{2}} \Delta t \end{aligned} \tag{32}$$

The boundary conditions are applied, and the data is written to an output file, along with the stresses, strains, yield stresses, and void contents for each integration point.

4. DAMAGE CONSTITUTIVE EQUATIONS

4.1 Gurson's Void Model

Yielding and plastic deformation in the element follows the model proposed by Gurson [3] for a symmetric deformations around a spherical void. The yielding condition is

$$\Phi = \left(\frac{q}{\sigma_0}\right)^2 + 2q_1 f \cosh\left(-\frac{3}{2}\frac{q_2 p}{\sigma_0}\right) - \left(1 + q_3 f^2\right) = 0 \qquad \textbf{(33)}$$

where f is the current porosity, p is the hydrostatic stress, q is the effective stress, and σ_0 is the current tensile yield stress. The constants q_1, q_2, and q_3 are constants introduced by Tvergaard [4] in order to provide a better match with numerical studies. Aravas [5] provides a detailed explanation of implementing this model in a static finite element algorithm. The procedure used here is essentially the same, with minor modifications due to the different element formulation. The stress is then transformed to local coordinates, and the internal force vector is computed as described above in section 2.6. One major benefit of using this model in Equation (33) is that if f is initially 0, the yielding criteria surface is identical to the von Mises yield condition. Addessio, et al., [6] discussed the importance of void growth and its effects on plastic deformation in high strain rate conditions, especially on the pressure wave propagation through the material. Therefore, this model is well suited to the application of ship-shock test simulation.

After calculating the strain tensor using Equations (24), any previous plastic strain is subtracted using

$$\{\epsilon^e\} = \{\epsilon^{total}\} - \{\epsilon^p\} \qquad \textbf{(34)}$$

The stress is then calculated using the components of $\{\epsilon^e\}$ in Equation (24). Using these values, the hydrostatic stress and effective stress are calculated as follows:

$$p = \frac{-1}{3}\left(\sigma_{xx} + \sigma_{yy} + \sigma_{zz}\right) \tag{35}$$

$$\{s\} = \{\sigma\} + p\{\delta\} \quad \{\delta\} = \{1\ 1\ 1\ 0\ 0\ 0\}^T \tag{36}$$

$$q = \sqrt{\frac{3}{2}\left(s_1^2 + s_2^2 + s_3^2 + 2\left(s_4^2 + s_5^2 + s_6^2\right)\right)} \tag{37}$$

At this point, Φ is calculated from Equation (33). If Φ is greater than 0, indicating plastic deformation, iteration is required to determine the new porosity and change in plastic strain. The predictor-corrector method used by Addessio, et. al. [6], is also used here. Using the values of p and q previously calculated as a first guess, correction factors are calculated using

$$\{C_f\} = [A]^{-1}\{A1\} \tag{38}$$

where

$$\{A1\} = \begin{Bmatrix} -\Phi \\ -\Delta\epsilon_p \frac{\partial\Phi}{\partial q} - \Delta\epsilon_q \frac{\partial\Phi}{\partial p} \end{Bmatrix} \tag{39}$$

$$[A] = \begin{bmatrix} K\frac{\partial\Phi}{\partial p} & -3G\frac{\partial\Phi}{\partial q} \\ \frac{\partial\Phi}{\partial q} + K\Delta\epsilon_q \frac{\partial^2\Phi}{\partial p^2} & \frac{\partial\Phi}{\partial p} - 3G\Delta\epsilon_p \frac{\partial^2\Phi}{\partial q^2} \end{bmatrix} \tag{40}$$

$$\{C_f\} = \begin{Bmatrix} \alpha \\ \beta \end{Bmatrix} \tag{41}$$

and

$$\frac{\partial \Phi}{\partial q} = \frac{2q}{\sigma_0^2} \qquad \frac{\partial^2 \Phi}{\partial q^2} = \frac{2}{\sigma_0^2}$$
$$\frac{\partial \Phi}{\partial p} = 2q_1 f\left(\frac{-3q_2}{2\sigma_0}\right)\sinh\left(\frac{-3q_2 p}{2\sigma_0}\right) \qquad \frac{\partial^2 \Phi}{\partial p^2} = 2q_1 f\left(\frac{3q_2}{2\sigma_0}\right)^2 \cosh\left(\frac{-3q_2 p}{2\sigma_0}\right) \tag{42}$$

The values for α and β are used to correct the change in strain caused by hydrostatic pressure and change in strain caused by effective stress, which are then used to determine the change in the plastic strain vector.

$$\begin{aligned} \Delta\epsilon_p^{new} &= \Delta\epsilon_p^{old} + \alpha \quad (\Delta\epsilon_p^0 = 0) \\ \Delta\epsilon_q^{new} &= \Delta\epsilon_q^{old} + \beta \quad (\Delta\epsilon_q^0 = 0) \end{aligned} \tag{43}$$

$$\{\Delta\epsilon^p\} = \tfrac{1}{3}\Delta\epsilon_p\{\delta\} + \Delta\epsilon_q\left(\frac{3}{2q}\right)\{s\} \tag{44}$$

This change in plastic strain, $\{\Delta\epsilon^p\}$, is then added to the strain calculated in Equation (34), and the stress vector is calculated again using Equations (24). Next, the change in void content is calculated as

$$\Delta f = \Delta f_{growth} + \Delta f_{nucleation} \qquad \Delta f_{growth} = (1-f)\sum \epsilon_{ii}^p \tag{45}$$

$$\Delta f_{nucleation} = \frac{f_N}{s_N\sqrt{2\pi}} \exp\left[-\frac{1}{2}\left(\frac{\epsilon^p - \epsilon_N}{s_N}\right)^2\right]\Delta\epsilon_p \tag{46}$$

where f_N is the volume fraction of void nucleating particles and ϵ_N and s_N are the mean and standard deviation of a normal distribution of nucleation strain, as suggested by Chu and Needleman [7], and utilized by Aravas [5]. These values are included in the input file element property matrix. Then the effective plastic strain, and void content are updated with

$$\Delta\epsilon^p = \frac{-p\Delta\epsilon_p + q\Delta\epsilon_q}{(1-f)\sigma_0} \qquad \epsilon^p_{t+\Delta t} = \epsilon^p_t + \Delta\epsilon^p \tag{47}$$

where ϵ^p_t is the effective plastic strain from the previous time step. At this point, the change in yield stress due to strain hardening is calculated, which is discussed in section 4.2. If either α or β is greater than a predetermined tolerance, the process iterates beginning with Equation (39). In practice, the above procedure is rarely required more than once due to the critical time step limitation of explicit time integration. The tolerance used is 1.0×10^{-4}. If the critical time step size is exceeded, the resulting stress will diverge towards infinity, and the iterative procedure outlined above will not converge. If the number of iterations exceeds a predetermined value, the element algorithm forces the program to terminate with an appropriate error message. Using a calculation time step size less than the critical time step size will allow convergence of the plastic deformation algorithm. During the iteration process, the updated values of effective plastic strain, $\Delta\epsilon_p$, $\Delta\epsilon_q$, f, and $\{\epsilon^p\}$ are retained and used as starting points for the next iteration.

4.2 Strain Hardening

Modeling the nonlinear elasto-plastic behavior of the material used is simplified by constructing a piece-wise linear version of the stress-strain plot. As written, the element will support up to 15 separate line segments to model the elasto-plastic region. Input requirements are further simplified by allowing the input of the tangent modulus, E_T, directly from the tensile-test stress-strain plot, and the upper strain limit of the region being modeled. The new yield stress is calculated with

$$\sigma_0^{t+\Delta t} = \sigma_0 + \sum_{i=1}^{j-1} E_{Ti}\left(\epsilon_i - \epsilon_{i-1}\right) + E_{Tj}\left(\epsilon_t^p - \epsilon_{j-1}\right) \quad \textbf{(48)}$$

where $\sigma_0^{t+\Delta t}$ is the yield stress for this time step, σ_0 is the original yield stress, ϵ_t^p is the effective plastic strain for the time step under consideration, and ϵ_i is the upper strain limit of the ith linear segment. ϵ_0 is the original yield strain, and is calculated by the program as simply $\frac{\sigma_0}{E}$. Figure 4 illustrates an example calculation.

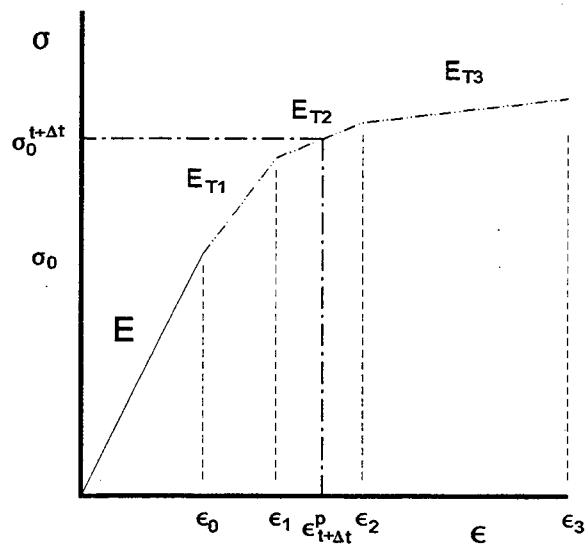

Figure 4. Calculating a New Yield Stress.

The effective plastic strain from Equation (47) is found to lie within the second plastic segment. The new yield stress is

$$\sigma_0^{t+\Delta t} = \sigma_0 + E_{T1}\left(\epsilon_1 - \epsilon_0\right) + E_{T2}\left(\epsilon_{t+\Delta t}^p - \epsilon_1\right) \quad \textbf{(49)}$$

The algorithm calculates the new yield stress as a function of the cumulative effective plastic strain and the original yield stress at each iteration.

Figure 4 also shows how the linear model for the elastic-plastic region is constructed. For most materials, three or four segments are sufficient to capture the strain-hardening behavior. The algorithm allows the user to input a negative tangent modulus, which is required to accurately model steels, necking, and failure (discussed in section 4.3). The material's behavior in compression is assumed to be identical to its behavior in tension. However, with only a minor modification to the program, a separate piece-wise linear model for compression could be included. The maximum number of linear segments has been arbitrarily set to fifteen, but this can also be readily increased to accommodate a more complex model.

A material that is ideally plastic after yielding is modeled by entering one linear segment of slope zero and an upper-limit strain higher than the expected strain. If the effective plastic strain of the element exceeds the upper-limit strain of the last linear segment, the yield stress will remain constant at the value of the endpoint of the last segment. No special indications are provided when this happens, so the stress-strain model should be defined for effective plastic strains well beyond those expected in the structure. An important property that is built into the strain hardening and plastic deformation algorithm is the retention of any previous plastic strain. If the external force is removed, the plastic strain will remain. As load is removed, the stress-strain plot will decrease at slope E from the new yield stress, and the new yield stress will remain in effect. If load is reapplied, plastic yielding will not occur again until the effective stress exceeds the new yield stress. For impact modeling, this property is vital to properly predict behavior as shock waves propagate back and forth through the material.

4.3 Failure

The strain hardening algorithm used in this element formulation also allows simple modeling of element failure. Since the strain hardening algorithm will accept negative values for tangent modulus, the stress-strain plot can be continued down to a stress of nearly zero in any manner that is appropriate to reflect the material's failure behavior. A final yield stress of zero is not currently supported, and will cause a divide by zero error, but can easily be

allowed if desired later. (The error will only occur if the element is strained to that point; the element will function normally at any strain below the point where the yield stress becomes zero). Since the material does not simply disappear when failure occurs, a small amount of yield stress should be retained to represent the momentum and stiffness of the remaining structure. Further study is required to determine an appropriate lower limit for this representative yield stress.

4.4 Storage Concerns

The damage constitutive equation model requires several key data from the previous time step in order to complete the calculations. The array used to pass the stress and strain values back to the time integration routine is also used to store the previous values of yield stress, porosity, effective plastic strain, and the plastic strain tensor (stored as a vector). The elastic stress and strain is simply written to an output file, and is not required for future calculations. A column vector of length 21 is required for each integration point: six elastic stress components, six elastic strain components, six plastic strain components, current yield stress, current porosity, and current effective plastic strain. The program structure currently supports up to a total of eight integration points per element. The basic formulation is designed for one in the x_1 and x_2 directions: the "center" of the element's plane surface. The number of integration points in the x_3 direction is user-defined in the input file. Currently, all elements must have the same number of integration points.

Several constants must be provided in the input file for this model: the initial void content, the constants *q1*, *q2*, and *q3*, the piecewise linear stress-strain relationship, and the distribution constants for void nucleation. The current implementation does not utilize default values, which are therefore provided by the preprocessor.

5. HOURGLASS MODE CONTROL

5.1 Hourglass Effects

In the standard formulation, the element is integrated fully along the x_3 direction, but is under-integrated in the x_1-x_2 plane. It is necessary to prevent shear-locking of the elements, which results in a structure that is too stiff. If any component of the applied force lies parallel to the x_1 - x_2 plane of any element in the structure, the zero energy mode of that element is excited enough to adversely affect the results. This excitation is quickly propagate to the surrounding elements, and eventually to the entire structure. These modes are referred to as "Hourglass Modes" due to the shape the structure takes on after complete propagation of this distortion. The impact of exciting these modes is to completely distort the structure in an unnatural manner, which renders any output data useless. In cases where the applied force does not sufficiently excite a zero energy mode, the analysis gives reliable results. When modeling a general curved structure, however, it is almost impossible to avoid exciting this mode. Figure 5 clearly illustrates the phenomenon using the pinched cylinder verification problem from section 6.3. In this case, the hourglass mode control built into the algorithm was disabled, and distortion in the structure is clearly visible.

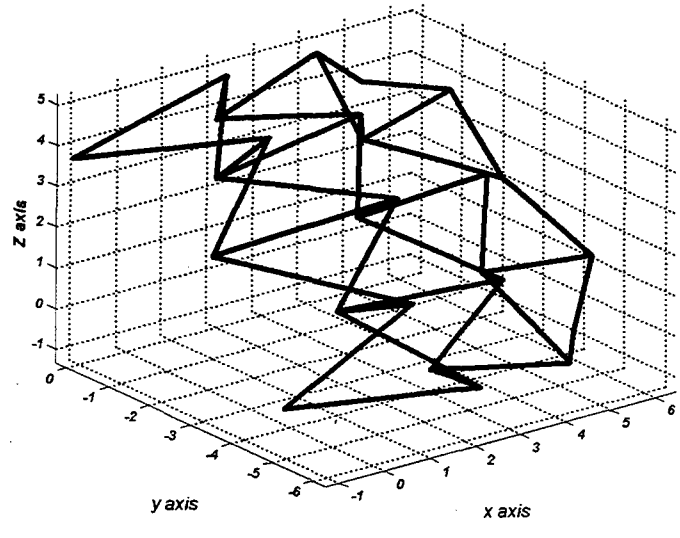

Figure 5. Pinched Cylinder without Hourglass Mode Control.

5.2 Method of Control

Belytschko, et al., [8] proposed an efficient means of controlling the hourglass modes of a similar element. The method described uses a portion of a stiffness matrix generated by full integration in all directions to modify the stiffness matrix generated by under-integration. Although this formulation does not use a stiffness matrix, a similar approach is just as effective in controlling these modes.

In this formulation, only one hourglass mode presents a problem, as shown in Figure 5. Rather than fully integrating in all three directions, the element is fully integrated in the x_1 - x_2 plane, but under-integrated in the x_3 direction. The relative location of the integration points used for hourglass control is shown in Figure 7. The procedure described in section 2 is followed to generate an internal force vector related to these four integration points.

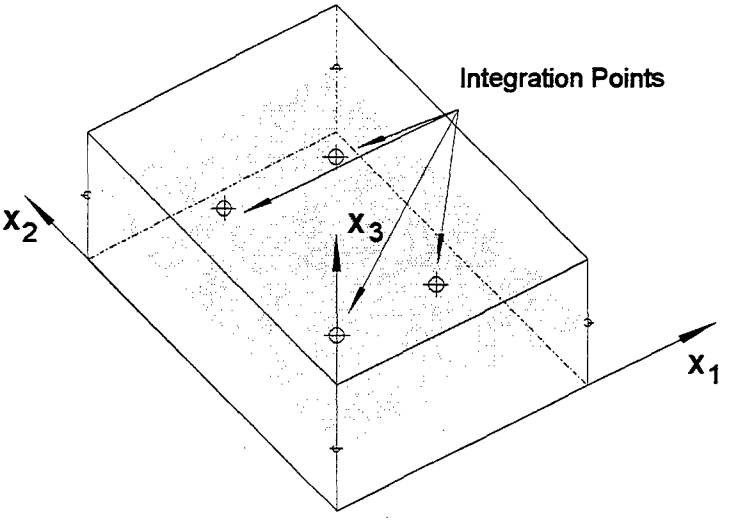

Figure 6. Hourglass Mode Control Integration Points.

The algorithm for calculating strain, stress, and then force for the hourglass mode control integration points is identical to the algorithm used to produce the main internal force vector, with the exception of plastic strain. No plastic strain is subtracted from the strain resulting from Equation (23), and the damage constitutive equations described in the previous section

are not utilized. The internal forces generated from the two integration schemes are treated like the stiffness matrices in Belytschko, et al. [7]. The new force vector is

$$\{f_{int}\} = \{f_{int}^{1x1x2}\} + h\{f_{hour}\} \tag{50}$$

where

$$\{f_{hour}\} = \{f_{int}^{2x2x1}\} - \{f_{int}^{1x1x2}\} \tag{51}$$

and

$$h = \frac{rt^2}{A} \tag{52}$$

The variable h is used here in Equations (50) and (51) instead of the ϵ used in Belytschko, et al. [7] to avoid confusion with the multiple strains required in this formulation. The variables used to calculate h are the element thickness (t) and the element's surface area (A). The effect of r follows that described in Belytschko, et al. [7], and is set to 0.05. The range of values for r that effectively controls the hourglass modes, but does not greatly effect the overall element stiffness is roughly 0.046 to 0.057 (determined experimentally). Since the elements are in arbitrary orientation in 3-D space, the area calculation is computed as the sum of the area of the two triangles formed by dividing the element at the diagonal between nodes 1 and 3:

$$A = \frac{1}{2}\sqrt{l_1^2 l_2^2 - D_1^2} + \sqrt{l_3^2 l_4^2 - D_2^2} \tag{53}$$

where

$$\begin{aligned} D_1 &= (x_1 - x_2)(x_3 - x_2) + (y_1 - y_2)(y_3 - y_2) + (z_1 - z_2)(z_3 - z_2) \\ D_2 &= (x_1 - x_4)(x_3 - x_4) + (y_1 - y_4)(y_3 - y_4) + (z_1 - z_4)(z_3 - z_4) \end{aligned} \tag{54}$$

$$
\begin{aligned}
l_1 &= \sqrt{(x_2 - x_1)^2 + (y_2 - y_1)^2 + (z_2 - z_1)^2} \\
l_2 &= \sqrt{(x_3 - x_2)^2 + (y_3 - y_2)^2 + (z_3 - z_2)^2} \\
l_3 &= \sqrt{(x_4 - x_3)^2 + (y_4 - y_3)^2 + (z_4 - z_3)^2} \\
l_4 &= \sqrt{(x_1 - x_4)^2 + (y_1 - y_4)^2 + (z_1 - z_4)^2}
\end{aligned}
\tag{55}
$$

and $(x_k\ ,\ y_k\ ,\ z_k\ )$ is the location of node k in the global coordinate system. For these calculations, the element is assumed to be flat (no curvature along either the x_1 or x_2 directions).

5.3 Effectiveness and Impact of Hourglass Mode Control

The hourglass mode control described was applied to the same pinched cylinder problem shown in Figure 5. The results are shown in Figure 7, which clearly demonstrates the effectiveness of the this method in controlling the zero energy modes. Both Figure 5 and Figure 7 use the same structure, applied force, calculation time step, and time step displayed.

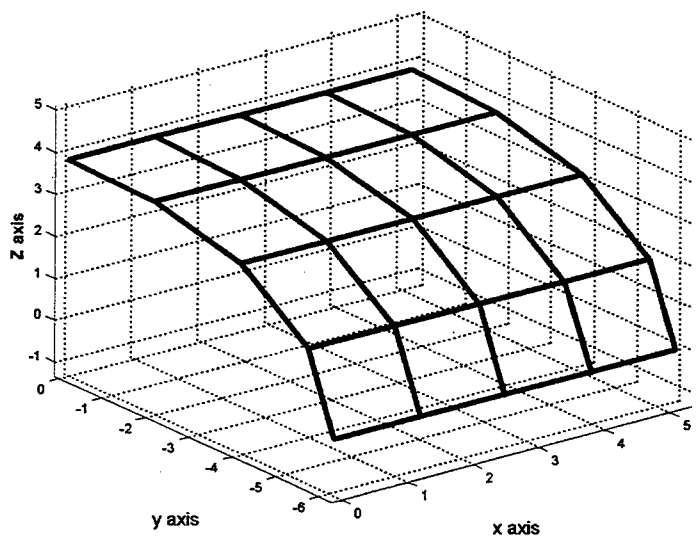

Figure 7. Pinched Cylinder with Hourglass Mode Control.

The additional error introduced by including hourglass control is sufficiently small that it does not alter the results significantly. All verification problems analyzed in the following section were completed with hourglass control enabled. The current implementation uses hourglass control consistently, but allows easy modification to make hourglass control a user-defined option.

One possible modification is to apply the hourglass control force every two or three time steps, vice every step. Another possibility is to apply hourglass control to selected elements, vice every element. Both modifications would reduce processing time, but require further study to determine if these changes would provide an adequate reduction in the hourglass modes.

6. VERIFICATION EXAMPLES

6.1 Transformation Matrix Verification

A cantilever plate is subjected to a tip load of 0.4 N distributed evenly along its width. The elastic modulus is 200 GPa, the density is 7850 kg/m^3, Poisson's ratio is 0.29, and the yield stress is 50 kPa. The plate is 2m x 2m x 10 cm thick. The problem is solved in four orientations: parallel to the x-y plane, parallel to the y-z plane, parallel to the x-z plane, and skew to all three planes. Two integration points through the thickness are used. Beam-bending theory gives a bending stress at the top integration point of 10.3923 kPa. All results are summarized in Table I, following the descriptions of each run.

Figure 8 shows the orientation for the first run. Nodes 1,2, and 3 are clamped, and the force is applied in the -z direction at nodes 7,8, and 9. Figures 9 and 10 show the displacement of the center tip node and the stress at the top integration point of element #1, respectively.

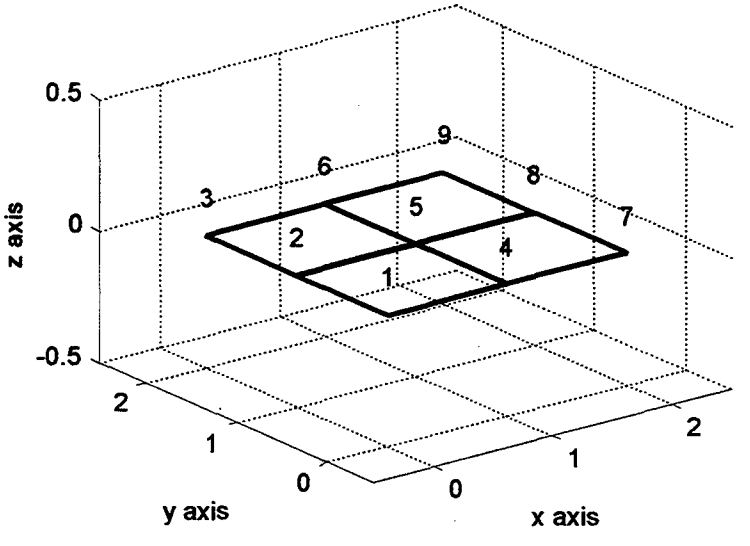

Figure 8. Cantilever Plate in the x-y Plane.

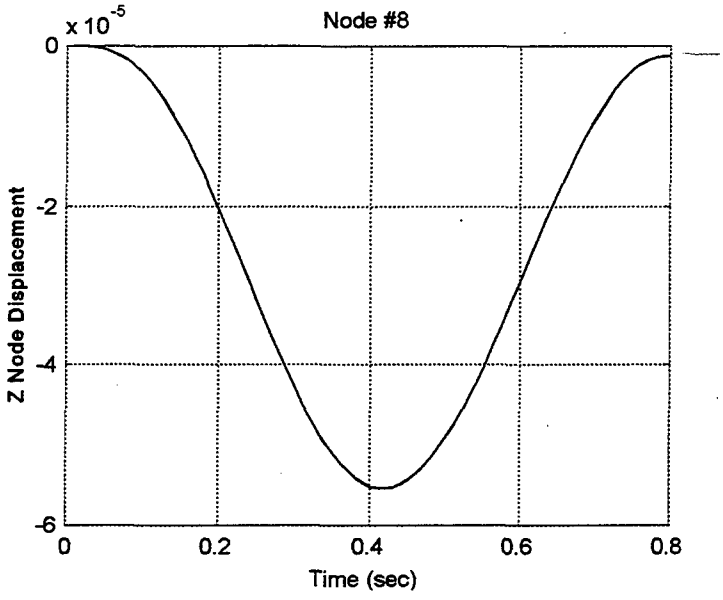

Figure 9. First Run Displacement History.

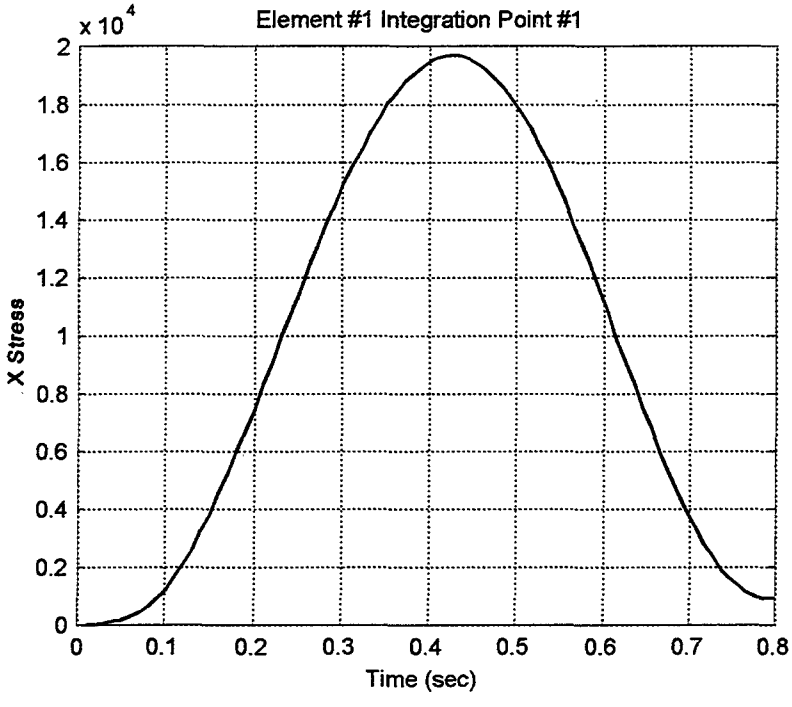

Figure 10. First Run Bending Stress History.

Figure 11 shows the orientation for the second run. Nodes 1,2, and 3 are clamped, and the force is applied in the x direction at nodes 7,8, and 9. Figures 12 and 13 show the displacement of the center tip node and the stress at the top integration point of element #1, respectively.

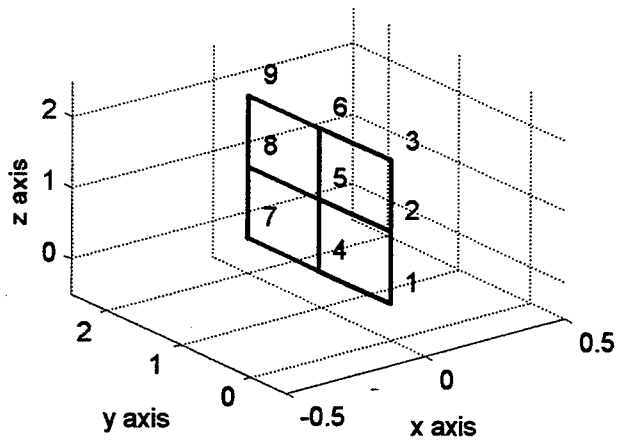

Figure 11. Cantelever Plate in the y-z Plane.

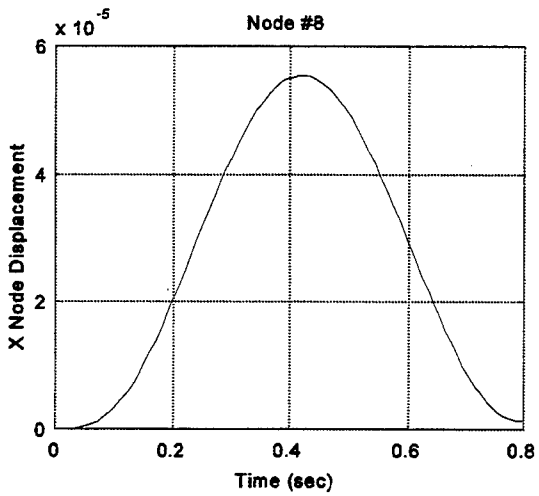

Figure 12. Second Run Displacement.

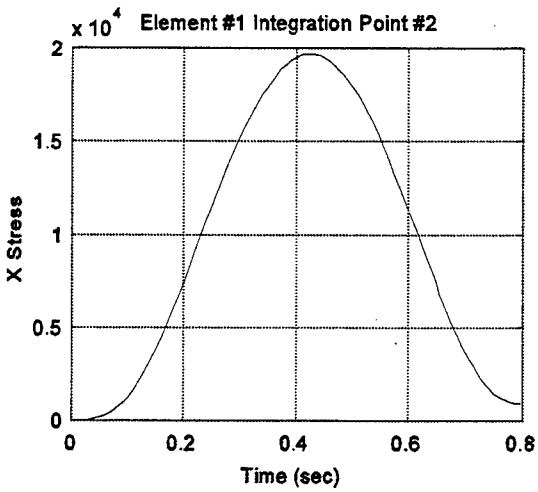

Figure 13. Second Run Bending Stress.

Figure 14 shows the orientation for the third run. Nodes 1,2, and 3 are clamped, and the force is applied in the -y direction at nodes 7,8, and 9. Figures 15 and 16 show the displacement of the center tip node and the stress at the top integration point of element #1, respectively.

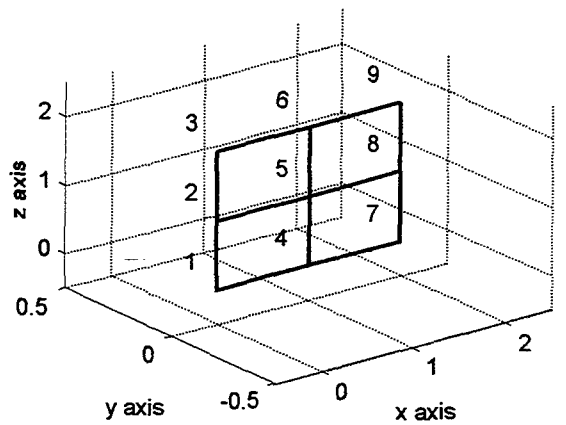

Figure 14. Cantilever Plate in the x-z Plane.

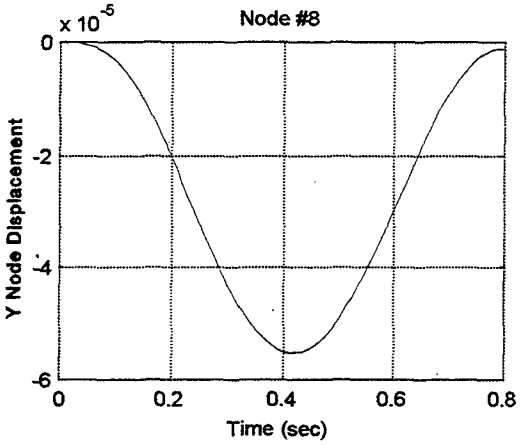

Figure 15. Third Run Displacement.

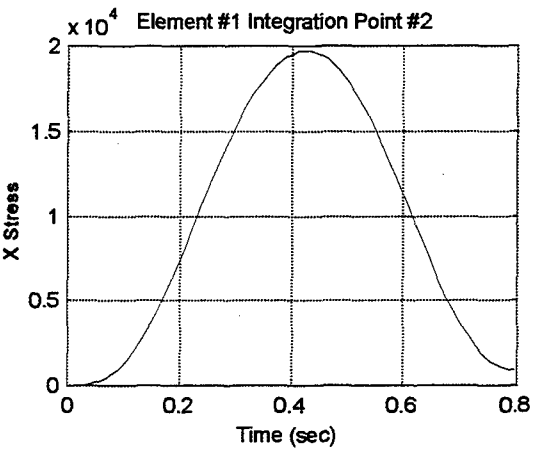

Figure 16. Third Run Bending Stress.

Figure 17 shows the orientation for the third run. Nodes 1,2, and 3 are clamped, and the force is applied in the -y direction at nodes 7,8, and 9. Figures 18 and 19 show the displacement of the center tip node and the stress at the top integration point of element #1, respectively.

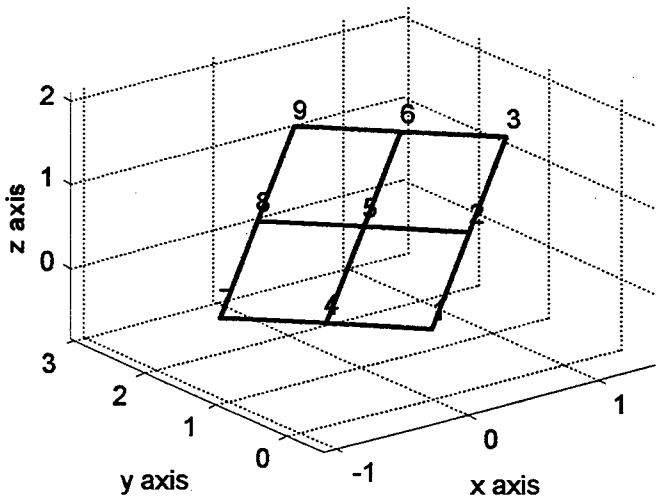

Figure 17. Cantilever Plate in Skew Orientation.

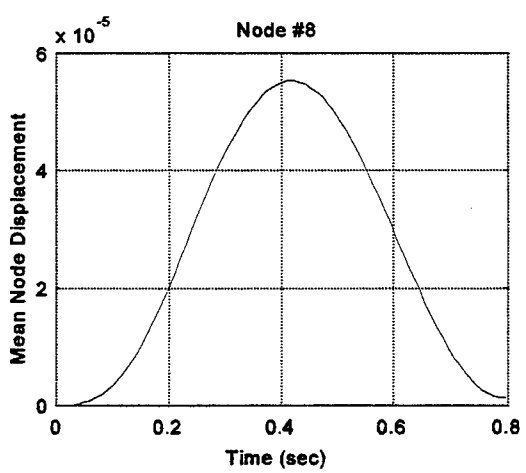

Figure 18. Fourth Run Displacement.

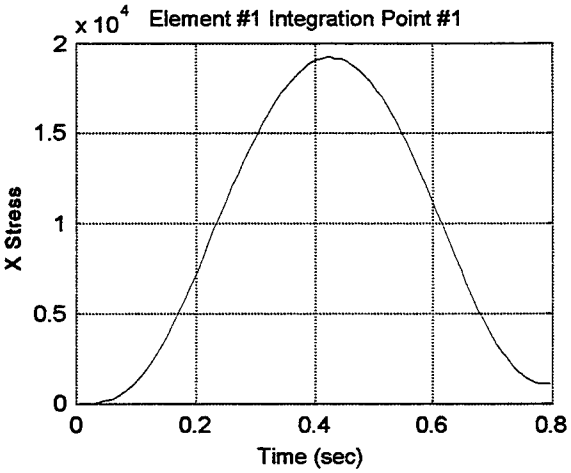

Figure 19. Fourth Run Bending Stress.

Table I summarizes the results for the four runs described above. The displacement and stress values are the means, calculated by dividing the peak value by two. The difference between run number four and the other runs is due to the accumulation round-off error in each component of the applied force and location of the nodes. The applied force had a magnitude of 0.3996 N, vice the 0.4 N used in the other problems. Note that the analytic solution assumes no stress across the width of the plate. The force was applied as a linear ramp from 0.0 N to 0.4 N over the time interval 0.0 seconds to 0.1 seconds, then held constant at 0.4 N, to prevent shock effects from influencing the results. This could not, however, remove all dynamic affects, and is the main source of error between the analytic and finite element solutions. The magnitude of the applied force was chosen to keep the effective stress throughout the structure well below the yield stress of the material, restricting the response to the elastic region.

TABLE I

Run Number	Orientation	Tip Displacement (m)	Bending Stress (kPa)
1	x-y Plane	27.6840×10^{-6}	9.839
2	y-z Plane	27.6840×10^{-6}	9.839
3	x-z Plane	27.6840×10^{-6}	9.839
4	Skew	27.6300×10^{-6}	9.608
Analytic	Static	29.3×10^{-6}	10.392

The results above demonstrate that the transformation matrices used in this formulation are effective in converting the displacements, strains, and stresses between the global and local coordinate systems.

6.2 Elastic Plate

A plate clamped on all four sides is subjected to a concentrated force at its center. The elastic modulus is 10 msi, the density is 0.1647 slugs/in^3, and Poisson's ratio is 0.2. The dimensions of the plate are 10 in x 10 in x 0.1 in thick. The yield stress is set high enough to ensure a completely elastic response. Two integration points through the thickness are used. The applied force is 40 lbf. The finite element mesh uses symmetry to model one quarter of the plate. Both a 2x2 (4 element) and 4x4 (16 element) mesh are used in the finite element analysis. Figure 20 shows the structure for the 4 element mesh.

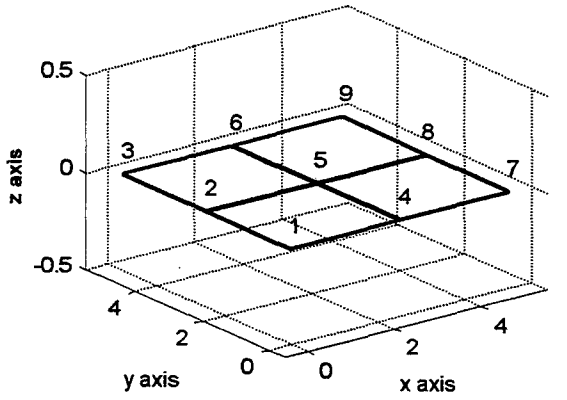

Figure 20. Clamped Plate 4 Element Mesh.

Nodes 1,2,3,4, and 7 are clamped. Nodes 6, 8, and 9 have symmetry conditions applied. The force is applied as a step of magnitude -10 lbf at node 9. The results for both meshes and the analytic solution are shown in Table II.

TABLE II

Analysis Type	Center Node Peak Displacement (in)
2x2 FE Mesh (Dynamic)	-4.74×10^{-2}
4x4 FE Mesh (Dynamic)	-4.94×10^{-2}
Analytic (Static times 2)	-4.90×10^{-2}

6.3 Pinched Cylinder

An open-ended cylinder of radius 5.0 in., length 10.35 in., and thickness 0.094 in. is subjected to a pinching load of 100 lbf. The elastic modulus is 10.5 msi, Poisson's ratio is 0.3125, and the density is 3.125×10^{-3} slugs/in^2. The load is applied as a step function beginning at time t = 0 seconds. Figure 21 illustrates the problem.

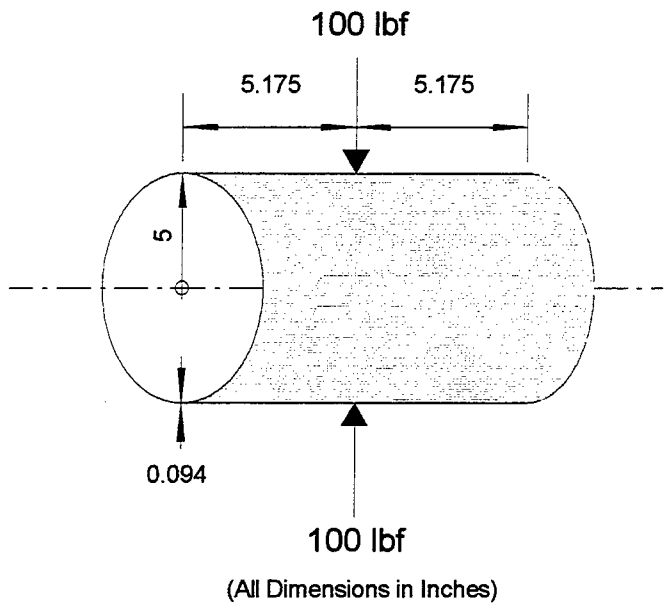

Figure 21. Pinched Cylinder Problem.

Using symmetry, the problem was reduced to a one-eighth section of the cylinder. The 16 element mesh used is shown in Figure 22. The deflection in the Z-direction of node number 25 is shown in Figure 23, which corresponds to the radial contraction of the cylinder. The dynamic value should be twice the analytic static value. Inextensional shell theory gives a static radial contraction of 0.1117 in. The maximum radial contraction of the model is 0.1995 in., which translates to a static radial contraction of 0.09975 in. Using a 256 element mesh (16 by 16), the maximum radial contraction was 0.2207 in., for a static contraction of 0.1104 in.

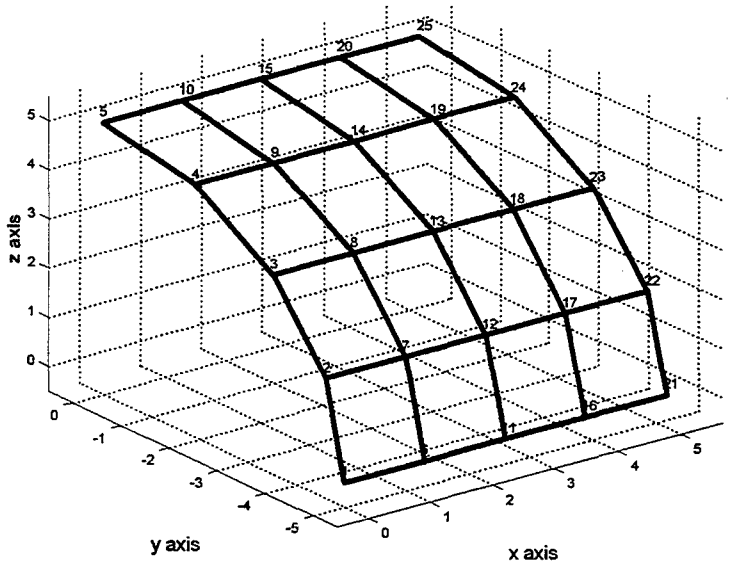

Figure 23. Pinched Cylinder Mesh.

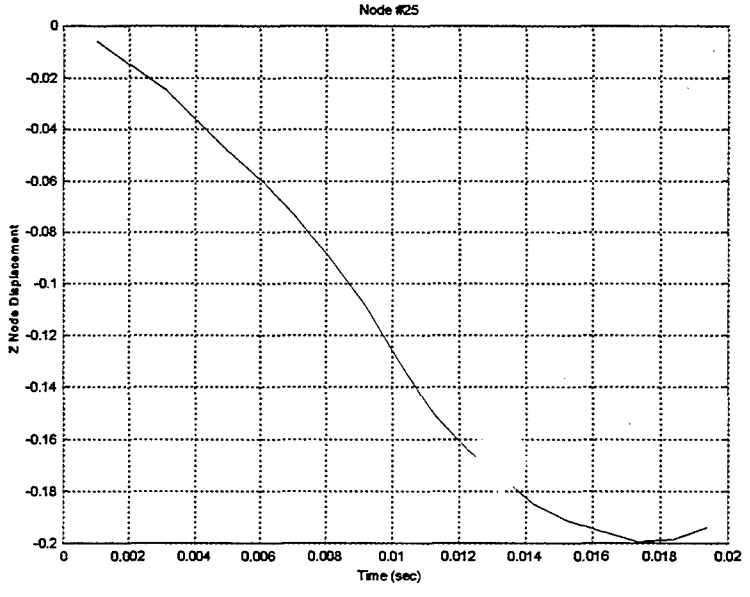

Figure 22. Pinched Cylinder Radial Contraction.

6.4 Elastic-Plastic Plate without Void Nucleation

A structural steel plate clamped on all four sides is subjected to a shock pressure in the form of a step with amplitude 60 kPa. The elastic modulus is 200 GPa, the density is 7850 kg/m^3, Poisson's ratio is 0.29, and the yield stress is 250 MPa. The stress-strain relationship will model the results of a typical tensile test. The plate dimensions are 9 m x 9 m x 1 cm thick. A 9 element mesh (3 x 3) will be used to model one quarter of the plate. The finite element mesh is shown in Figure 24. Nodes 1, 2, 3, 4, 5, 9, and 13 are clamped. The remaining boundary nodes have appropriate symmetry conditions applied.

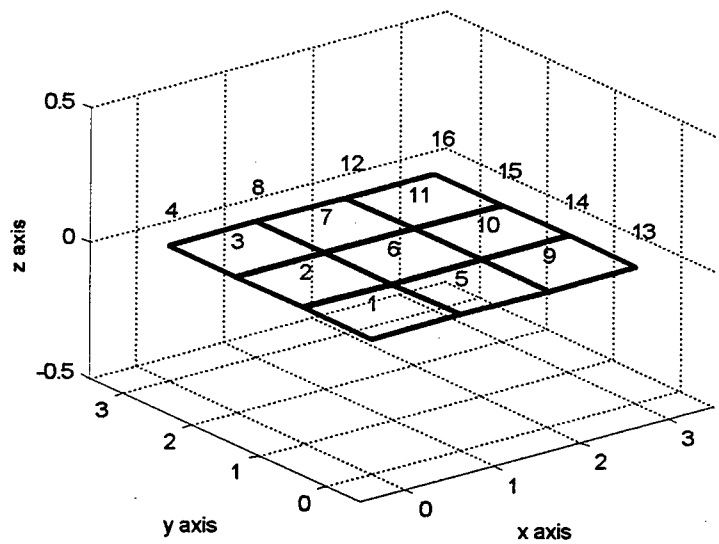

Figure 24. Finite Element Mesh for Elastic-Plastic Plate.

The stress-strain curve for the lower strain region is shown in Figure 25. A larger region of the stress-strain curve is shown in Figure 26. This problem is designed so as not to exceed the maximum stress of the strain-hardening region.

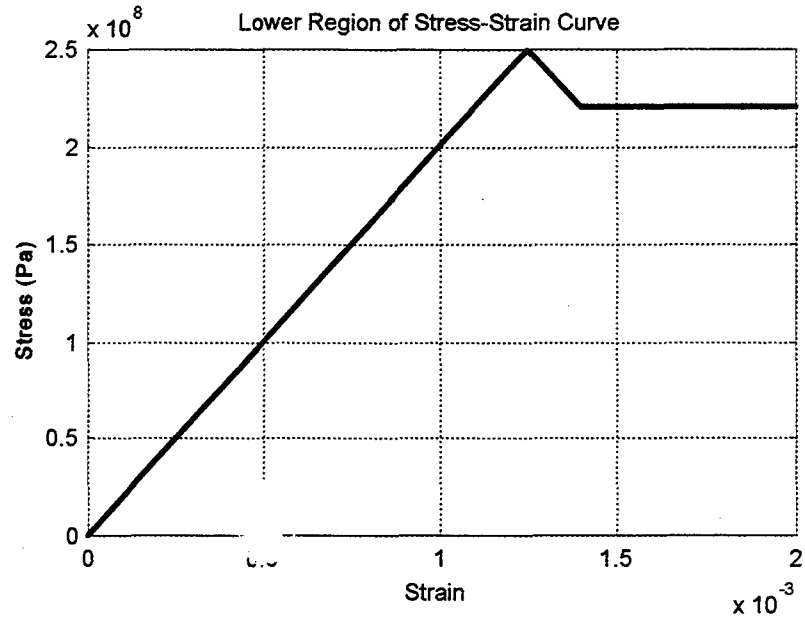

Figure 26. Structural Steel Stress-Strain Curve.

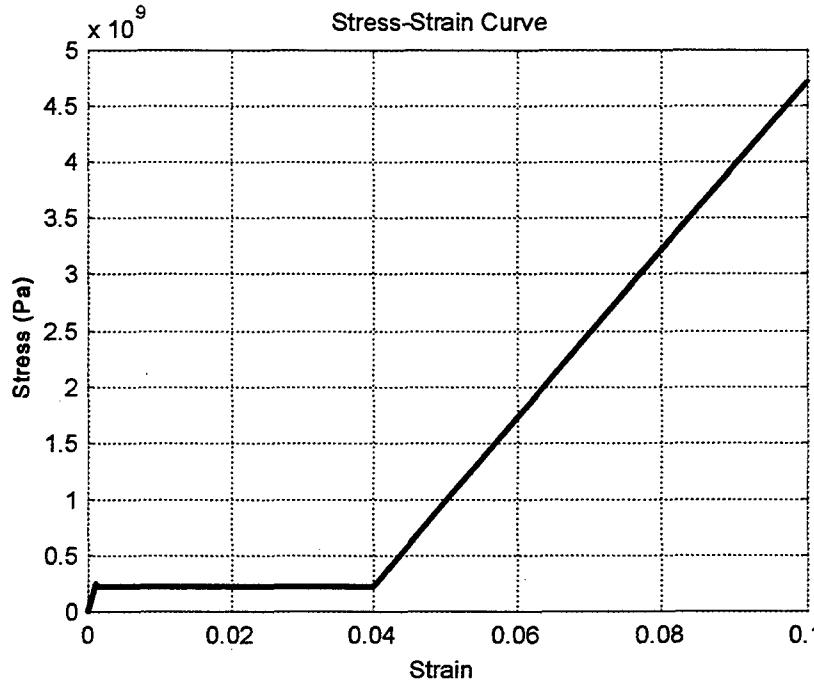

Figure 25. Structural Steel Stress-Strain Relationship.

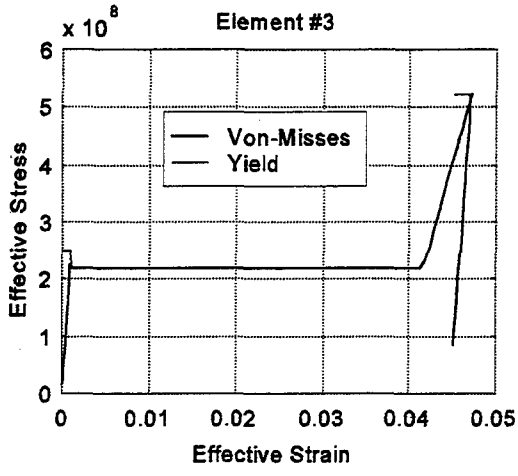

Figure 27. Stress-Strain at Top Integration Point.

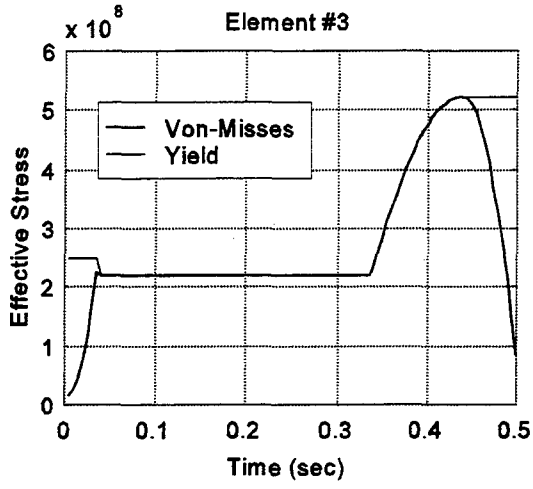

Figure 28. Stress History at Top Integration Point.

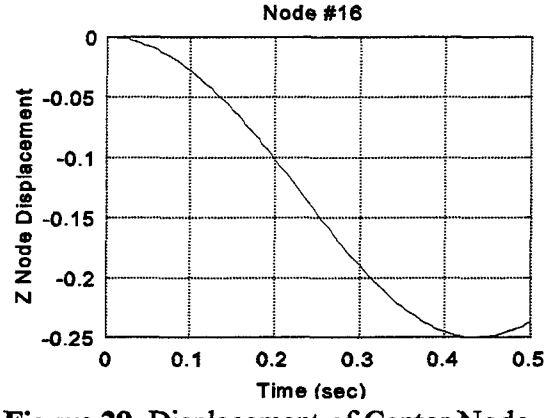

Figure 29. Displacement of Center Node.

Figures 27 through 29 show the results of the finite element analysis. The effectiveness of the strain hardening implemenation is shown in Figures 27 and 28. With microvoid effects disabled, the stress-strain curve follows the tensile test curve exactly. Note in Figure 27 that the stress follows the elastic modulus down as stress is relieved after the peak displacement.

6.5 Elastic-Plastic Plate with Void Growth and Nucleation

The problem of section 6.4 is repeated with the microvoid effects included. The constants for Equation (33) are: $q_1 = 1.5$, $q_2 = 1.0$, and $q_3 = 2.25$ (q_1^2). The initial porosity is 0.0. The density of nucleating particles (f_N) is 4%, the mean strain for nucleation (ϵ_N) is 0.3 with a standard deviation (s_N) of 0.1. These are the values recommended by Tvergaard [4] and Aravas [5]. All other parameters are identical to the problem described in section 6.4.

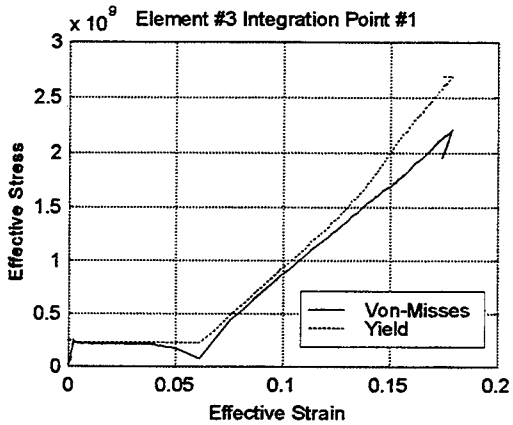

Figure 30. Stress-Strain Plot at Top Integration Point.

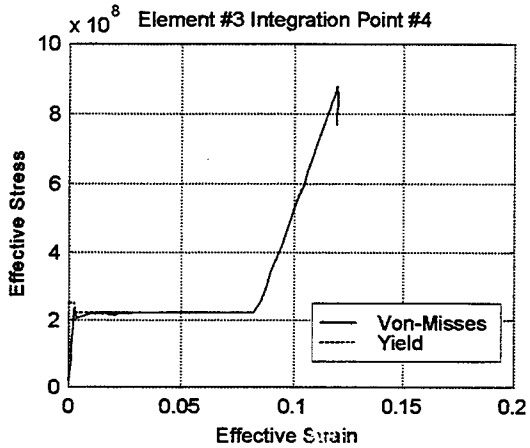

Fig 31. Stress-Strain Plot at Bottom Inte ion Point.

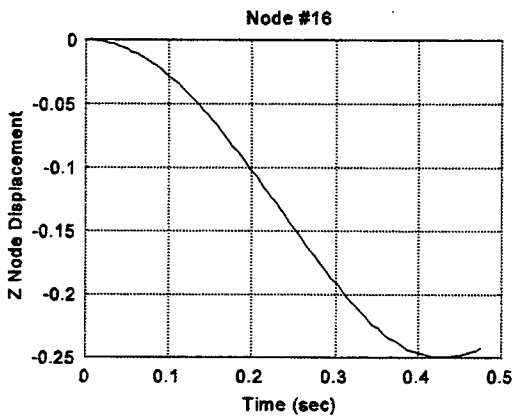

Figure 33. Center Node Displacement.

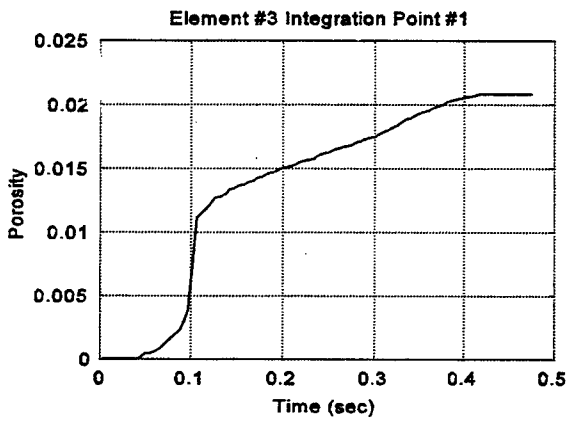

Figure 32. Void Nucleation and Growth.

Figures 31 and 32 show the effect of microvoids on effective stress. Figure 31 shows the stress-strain relationship in the top integration point of element #3. This fiber of the element is in tension, and voids quickly nucleate and grow during plastic deformation, as shown in Figure 34. Figuer 32 shows the stress-strain relationship at the bottom integration point of the same node. Since this fiber is in compression, there is no void nucleation, and the peak stress is significantly less than in the fiber in tension. Comparing Figure 33, center node displacement, with the center node displacement where void nucleation is disabled (Figure 30), illustrates that the peak displacement response is virtually unaffected by the introduction of microvoids. However, as Figure 32 shows, the element experienced significant additional plastic deformation and strain hardening. The top fiber of this element is much closer to failure than the corresponding fiber in the problem where microvoid effects are ignored.

8. CONCLUSIONS

With the exception of the issues noted below, the second phase of this research is complete. The formulation described in Kwon [1] has been implemented, with some modifications, into a dynamic finite element analysis program and verified. Damage constitutive equations have been incorporated, as well as Gurson's void model. The effect of void growth and nucleation on the model has been demonstrated, but further verification of the results is still required.

The values for the constants q_1, q_2, and q_3 used in Gurson's model are determined by the strain hardening exponent, as described in Tvergaard [4]. A method for determining appropriate values for a given piecewise linear model needs to be defined. Incorporating such a method into the implementation will help simplify problem definition, and reduce the number of constants the user must provide.

The constants for void nucleation (f_N, ϵ_N, and s_N), however, are dependent on material type and manufacturing process. Typical values for a variety of materials should be provided, along with recommended default values.

The robustness of the current implementation of the damage constitutive equations has not been verified. Although this shell element has been used to analyze over 20 different problems, further testing over a wider range of input conditions is needed to ensure consistency. Comparing the analysis results to experimental data, rather than the results of other models, should also be accomplished to verify accuracy and reliability.

Work can begin on the subsequent phase of this research, incorporating the element into the DYSMAS and/or DYNA3D program, concurrently with work on the refinements mentioned above. The current implementation is matched to a general purpose finite element analysis program. All applicable portions of the code will be extracted and modified as necessary to create a compatible module for the target program.

REFERENCES

[1] Y. W. Kwon, "Development of a Shell Element with Pressure Variation Through the Thickness", prepared for Naval Surface Warfare Center, Carderock MD, 1997.

[2] R. D. Cook, Concepts and Applications of Finite Element Analysis, 2nd ed. (New York: Wiley, 1981) 148-151.

[3] A. L. Gurson, "Continuum Theory of Ductile Rupture by Void Nucleation and Growth: Part I - Yield Criteria and Flow Rules for Porous Ductile Materials", Journal of Engineering Material Technology, 99, 2-5 (1977).

[4] V. Tvergaard, "Influence of Voids on Shear Band Instabilities under Plane Strain Conditions", International Journal of Fracture Mechanics, 17, 389-407 (1981).

[5] N. Aravas, "On the Integration of a Class of Pressure-Dependent Plasticity Models", International Journal for Numerical Methods in Engineering, 24, 1395-1416 (1987).

[6] F. L Addessio, J. N. Johnson, and P. J. Maudlin, "The Effect of Void Growth on Taylor Cylinder Impact Experiments", Journal of Applied Physics, 73.11, 7288-7297 (1993).

[7] C. C. Chu and A. Needleman, "Void Nucleation Effects in Biaxially Stretched Sheets", Journal of Engineering Material Technology, 012, 249-256 (1980).

[8] T. Belytschko, C. S. Tsay, and W. K. Liu, "A Stabilization Matrix for the Bilinear Mindlin Plate Element", Computer Methods in Applied Mechanics and Engineering, 29, 313-327 (1981).

INITIAL DISTRIBUTION LIST

		No. of Copies
1.	Defense Technology Information Center Cameron Station Alexandria, Virginia 22304-6145	2
2.	Dudley Knox Library, Code 52 Naval Postgraduate School Monterey, California 93943	2
3.	Professor Young W. Kwon, Code ME/Kw Naval Postgraduate School Monterey, California 93943	2
4.	Mr. John McKirgan, Code 614 Naval Surface Warfare Center Carderock Division 9500 MacArthur Boulevard West Bethesda, Maryland 20817-5700	1
5.	Mr. Edward Johnson Naval Surface Warfare Center Indian Head Division Code 40E, Bldg 302 Indian Head, Maryland 20640-5035	1
6.	LT Patrick M. McDermott, USN, Code 570/NE73 Naval Postgraduate School Monterey, California 93943	1
7.	Research Office, Code 09 Naval Postgraduate School Monterey, California 93943	1